Title
Sequence-Dependent Structural Stability of Self-Assembled Cylindrical Nanofibers by Peptide Amphiphiles

Journal
Biomacromolecules, 16(7)

ISSN
1525-7797

Authors
Fu, Iris W
Nguyen, Hung D

Publication Date
2015-07-13

DOI
10.1021/acs.biomac.5b00595

Peer reviewed

Article

pubs.acs.org/Biomac

Sequence-Dependent Structural Stability of Self-Assembled Cylindrical Nanofibers by Peptide Amphiphiles

Iris W. Fu and Hung D. Nguyen*

Department of Chemical Engineering and Materials Science, University of California, Irvine, Irvine, California 92697, United States

Supporting Information

ABSTRACT: Three-dimensional networks of nanofibers, which are formed through self-assembly of peptide amphiphiles, serve as a biomimetic hydrogel scaffold for tissue engineering. With an emphasis to improve hydrogel properties for cell-specific behavior, a better understanding between structural characteristics and physical properties of the macroscopic gel is sought. Large-scale molecular dynamics simulations were performed on two PA sequences with identical composition (palmitoyl-$V_3A_3E_3$ and palmitoyl-$A_3V_3E_3$) showing different self-assembly kinetic mechanisms. While both sequences yielded cylindrical nanofibers, these structures have contrasting internal arrangement with respect to the hydrophobic core; the former is continuous with predominately alkyl tails, whereas the latter is disjointed with interconnecting micelles. Two additional sequences (palmitoyl-V_6E_3 and palmitoyl-A_6E_3) were examined to determine the effects of a homogeneous β-sheet forming segment that is either strongly or mildly hydrophobic on self-assembly. Results from this study indicate that internal structural arrangement of nanofibers can provide a correlation with structural stability and mechanical behavior of hydrogel nanostructures.

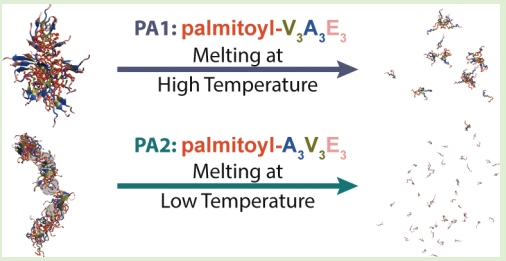

1. INTRODUCTION

Design strategies for self-assembling amphiphilic peptides have embraced a modular approach that yields nanostructures with highly specific structural properties[1−3] and biofunctionalities.[4−6] As surfactant-like peptides, peptide amphiphiles (PAs) are an emerging class of biomaterials that are able to undergo spontaneous conformational transitions as a result of local environmental changes.[7−10] These molecules primarily encompass two fundamental elements to promote gelation and self-assembly: a relatively short hydrophilic peptide sequence that is attached to a synthetic hydrophobic group.[11−13] From this template, numerous variations have been made including the use of multiple hydrophobic fatty acid attachment,[14−16] modification of peptide sequence,[17,18] and incorporation of site-specific bioactive epitopes[19−21] for a broad range of applications such as diagnostic medicine, controlled and targeted drug delivery, tissue engineering, and nanofabrication.[22−25] However, while it is known that certain desired characteristics are attributed to specific noncovalent interactions through structural modifications, rational design and systematic understanding remains incomplete.

The self-assembly of a network of fibrillar nanostructures from PA molecules has been shown to be a promising biomimetic hydrogel scaffold.[24,26] Individual fibrillar nanostructures are characterized by cylindrical nanofibers that exhibit β-sheet elements on the surface with a hydrophobic core.[2,11] Early design principles of PA molecules have primarily emphasized structural modifications to improve biocompatibility or to minimize immunogenic properties;[11,27] however, with the aims to use PA self-assembled nanostructures as a synthetic hydrogel scaffold that mimics extracellular matrix, consideration is also placed on the relationship between structural characteristics and mechanical behavior. For example, modifying the mechanical rigidity of hydrogels serving as extracellular matrix results in different cell adhesion and cell differentiation behaviors.[28−30] To incorporate this additional design parameter for PA molecules, experimental studies have found that the stiffness of the gel can be correlated with the presence of secondary structure β-sheet elements, which is attributed to increased intermolecular hydrogen bonding and structural stability.[17,31] Similar trends have also been observed for amphiphilic peptide systems to relate secondary structure formation to mechanical strength and subsequent molecular arrangement properties.[20,32−37] Consequently, the ability to exert control and influence the morphological outcome of PA self-assembled nanostructures provides a platform to study in-depth the relationship between structural features and bulk material properties.

The particular choice and arrangement of hydrophobic residues have been shown to affect not only the supramolecular architecture[38,39] but also the corresponding gel stiffness.[40,41] For PA molecules that have a palmitic alkyl tail ($C_{16}H_{31}O$- or palmitoyl), sequence patterns have been designed to manipulate the hydrophobic-to-hydrophilic ratio to determine the impact on self-assembly behavior. Using a systematic approach and keeping the number of residues constant in the β-sheet forming region, Pashuck et al. designed three PA sequences, $V_4A_2E_3$, $V_3A_3E_3$, and $V_2A_4E_3$ to examine the effect

Received: May 2, 2015
Revised: June 9, 2015

DOI: 10.1021/acs.biomac.5b00595
Biomacromolecules XXXX, XXX, XXX−XXX

of decreasing the number of strong β-sheet formers.[17] As the number of strong β-sheet formers is decreased, rheological measurement of the storage modulus shows a decreasing trend indicative of weaker gel formation. This effect corroborates with the lowered propensity to form intermolecular hydrogen bonds, which can contribute to minimizing the rigidity of the nanostructure. Similar decreases in gel stiffness are also observed when the total number of hydrophobic residues is reduced proportionally using $V_4A_4E_3$, $V_3A_3E_3$, and $V_2A_2E_3$. In the same study, Pashuck et al. examined the effect of strong β-sheet former placement with respect to the position of the alkyl tail.[17] For two PA sequences with identical composition, $V_3A_3E_3$ and $A_3V_3E_3$, placement of the strong β-sheet former, valine, further away from the alkyl tail decreased the gel stiffness by a surprising 1 order of magnitude. Although both sequences formed characteristic nanofibril structure with comparable β-sheet formation, it was hypothesized that the difference in mechanical property was attributed to twistedness from misaligned and hyperextended hydrogen bonding. Although the aforementioned studies suggest that selective placement of individual residues can provide an additional strategy to influence self-assembly behavior, the weighted contribution from different noncovalent interactions (e.g., hydrophobic interaction, hydrogen bond, electrostatic repulsion) is difficult to evaluate, prompting for more studies to elucidate such effects at a molecular level.

In this article, we perform molecular dynamics simulations using our coarse-grained ePRIME model,[42] which permits spontaneous formation of hydrogen bonds and secondary structures. These simulations are truly large-scale on multiple systems that contain 800 PA molecules, which is at least 10 times larger than a typical simulation involving short peptides using other coarse-grained models.[43] By interchanging blocks of hydrophobic residues with one another with respect to the position of the palmitic alkyl tail, our studies showcases the subtle differences in the molecular arrangement to correlate with the experimental differences observed in mechanical properties. The sequences (Table 1) examined in this work,

Table 1. PA Sequences

	sequence
PA molecule	alkyl tail−β-sheet region−charged region
PA1	$C_{16}H_{31}O$−VVVAAA−EEE
PA2	$C_{16}H_{31}O$−AAAVVV−EEE
PA3	$C_{16}H_{31}O$−VVVVVV−EEE
PA4	$C_{16}H_{31}O$−AAAAAA−EEE

PA1: palmitoyl-$V_3A_3E_3$ and **PA2:** palmitoyl-$A_3V_3E_3$, are based on prior experimental work by Pashuck et al.[17] From our simulation studies, we found that the difference between the two sequences is attributed to the packing geometry as a result of the increased hydrophobic interaction between the peptide sequence and the alkyl tail. The core of the nanofibril structure is found to be less continuous when the strong hydrophobic block (valine) is placed further away from the alkyl tail. Two additional sequences, **PA3:** palmitoyl-V_6E_3 and **PA4:** palmitoyl-A_6E_3 (Table 1) were also examined to determine the effects of using a homogeneous β-sheet forming segment that is either strongly or mildly hydrophobic. From these four PA sequence variants and their influence on the corresponding self-assembly behavior, a better understanding can be gained regarding the role of the β-sheet forming region. We aim to provide further insight and intuition to customize sequences with desired structure and functionality. Having previously examined the effects of pH-dependent electrostatics[10,42] and solvent-dependent hydrophobicity[44,45] on the formation of hydrogel nanostructures, this study of sequence effects adds a more comprehensive understanding of PA self-assembly.

2. METHODS

Two short PA sequences (Table 1) represented as **PA1**: palmitoyl-$V_3A_3E_3$ and **PA2:** palmitoyl-$A_3V_3E_3$, are examined in which the chemical identity and composition remains identical with the exception of the sequence pattern arrangement within the β-sheet forming segment. These two sequences were chosen based on previous experimental work by Pashuck et al.[17] Two additional sequences, **PA3:** palmitoyl-V_6E_3 and **PA4:** palmitoyl-A_6E_3, are considered to determine the effects of using a homogeneous β-sheet-forming segment by extending the length of a single hydrophobic residue that is either strongly or mildly hydrophobic. Each PA molecule is represented using a coarse-grained model ePRIME,[42] an extension of the Protein Intermediate Resolution Model (PRIME),[46−48] that accounts for all 20 naturally occurring amino acids. For the peptide residues, three spheres are used to represent the backbone atoms: amide, α carbon, and carbonyl groups (NH, $C_\alpha H$, and CO, respectively). The corresponding amino acid side chains is either represented with either one or two spheres based on the length of the side chain based on the scheme originally developed by Wallqvist and Ullner.[49] The size of a side chain sphere is derived from the solvent accessible area experimentally determined by Wesson and Eisenberg.[50] For the hydrophobic palmitoyl tail, each CH_2 group is represented as a single sphere whose bond distance and fluctuation are extracted from available atomistic parameters.[42]

For the system of interest, an implicit solvent model is implemented to reduce the system's size to allow for tractable simulations in order to capture the whole spontaneous self-assembly process. The solvent effect is incorporated into the effective residue−residue potential based on the hydrophobic or hydrophilic character of the corresponding peptide residue or alkyl group. Representation of this behavior is either through a square-well or square-shoulder potential that approximates an attractive or repulsive continuous potential, respectively. For example, square-well potential is used for attractive interactions between hydrophobic side chains and/or polymeric segments, whereas square-shoulder potential is used for repulsive interactions between hydrophilic side chains or polymeric segments. The strength of the interaction between two groups is $\varepsilon_{HP} = R(\Delta G_i + \Delta G_j)$,[50,51] where ΔG is the free energy of transferring each group from water to octanol, and R is a measure of the strength of the hydrophobic interaction. In this study, the value for R, which is interpreted as the degree of hydrophobicity between nonpolar groups and is governed by the particular solvent choice, is kept constant at $R = 1/3$ based on prior work in our group that has established this reference condition for the formation of prototypical cylindrical nanofibers.[42,44,45] Comparison of our structures[42] showed a high degree of similarity with those observed in experimental structures.[2,12] Moreover, the simulations that were conducted by the Schatz group using atomistic and coarse-grained models[52−54] with explicit solvents produce similar structures as those observed by our simulations. This evidence validates our use of implicit solvent model without biasing the results of the self-assembling behavior.

Hydrogen bonding is represented by a directionally dependent square-well attraction of strength ε_{HB} = 12 kJ/mol between the NH and CO united atoms. Electrostatic interactions, which are treated at the level of Debye−Huckel theory, are implemented using three-step attractive square-well or repulsive shoulder-well potentials with a 12 Å cutoff. In this study, the strength of an electrostatic repulsion between two charges on the glutamic acids, ε_{ES}, is the same as that of the hydrogen bond, ε_{HB}, as it is the optimal condition where cylindrical nanofibers were observed in our previous study.[42]

In conjunction with the coarse-grained representation of the system, discontinuous molecular dynamics (DMD) is utilized to enable

DOI: 10.1021/acs.biomac.5b00595
Biomacromolecules XXXX, XXX, XXX−XXX

simulations of large system sizes and extended time scales. As an alternative to standard molecular dynamics, DMD models bonded and nonbonded interactions through discontinuous potentials (e.g., hard-sphere and square-well potentials). Unlike soft potentials, such as the Lennard−Jones potential, discontinuous potentials exert forces only when particles collide, enabling the exact (as opposed to numerical) solution of the collision dynamics. DMD simulations proceed by locating the next collision, advancing the system to that collision, and then calculating the collision dynamics. By reducing the interaction details that is needed by being an event-driven process as opposed to a time-driven process, this type of simulation allows for greater time scales on large systems. Simulations are performed in the canonical ensemble (NVT) with periodic boundary conditions imposed to eliminate artifacts due to box walls. Constant temperature is achieved by implementing the Andersen thermostat method.[55] In this case, all beads are subjected to random, infrequent collisions with ghost particles whose velocities are chosen randomly from a Maxwell−Boltzmann distribution centered at the system temperature. Simulation temperature is expressed in terms of the reduced temperature, $T^* = k_B T/\varepsilon_{HB}$, where k_B is Boltzmann's constant and T is the temperature. Reduced time is defined to be $t^* = t/\sigma(k_B T/m)^{1/2}$, where t is the simulation time and σ and m are the average bead diameter and mass, respectively. While the use of reduced quantities *in silico* poses difficulty in achieving an experimental analogue, qualitative correlations can be extracted. From earlier work examining single-molecule behavior using both atomistic and coarse-grained models,[42,56] a qualitative frame of reference can be identified correlating the melting temperature of $T^* = 0.085$ to T ∼ 320 K.

The initial configuration of each simulation contains 800 PA molecules (44 000 particles) in a cubic box whose dimension is 250 Å. This initial configuration was randomized to remove any biased conformations by heating the system at a high temperature ($T^* = 5.0$) for a short amount of time (<1% of production run) to mimic experimental conditions. Afterward, the system was quickly quenched to $T^* = 0.11$, which is the final temperature for the production run for around 200 time units until reaching equilibrium. The criteria for equilibrium is that each simulation was conducted for a long period of time until the ensemble averages of the system's total potential energy varied by no more than 2.5% during the last three-quarters of each simulation run. The sudden change in temperature should have negligible effects on the system properties, as the randomization is used only for the purpose of removing any computational bias due to the technique of populating the initial system with PA molecules. From our previous study on the effects of temperature,[42] we found that below and at the melting point of $T^* = 0.085$ PAs formed kinetically trapped aggregates that are amorphous. At higher temperatures, $T^* = 0.10$−0.11, cylindrical nanofibers can be formed when $R = 1/3$. Similarly, Lee et al.[54] conducted their simulations observing the formation of nanofibers at 330 K, which is slightly higher than the melting point. In this study, the temperature is constant at $T^* = 0.11$.

Quantitative analysis in this paper was performed on the data collected during the production period. Average properties at equilibrium were computed from the last 10% of simulation data with error bars taken from the standard deviation of at least five independent simulations for **PA1** and **PA2**, and at least two independent simulations for **PA3** and **PA4**. Multiple independent simulations were performed considering the stochastic nature of self-assembly; however, results indicate that variability in the data is relatively minimal. Calculation of the secondary structure present in the system is through the implementation of STRIDE,[57] with primary focus on α-helix, β-strand/sheet, and random coil that also contains turn structures. To identify an aggregate formed during the trajectory of the simulation, individual PA molecules of a cluster must form at least two interpeptide hydrogen bonds or four hydrophobic interactions with a neighboring PA molecule in the same group.[47] This criterion ensures that an aggregate is defined by at least two or more PA molecules to form enough stable interactions.

Calculation of the PA molecule's velocity is reported based on the 13 individual regions of the molecule itself. The 16-hydrocarbon alkyl tail is parsed into four equal regions with the remaining nine regions corresponding to each of the peptide residue. The velocity was calculated for the entire 800-PA molecule system and averaged over the independent simulations. Lindemann criterion was calculated along the length of the fiber axis for a representative aggregate identified in the 800-PA molecule system. A total of 25 regions were chosen along the length of the fiber axis of the nanostructure to compute the Lindemann criterion to obtain information in localized regions. The evaluation of the Lindemann criterion is determined by using eq 1.

$$\Delta_L = \frac{\sqrt{\sum_i \langle (\mathbf{r}_i - \langle \mathbf{r}_i \rangle)^2 \rangle / N}}{a'} \quad (1)$$

The total number of atoms is represented by N, and a' is the most probable nonbonded near neighbor distance; $\mathbf{r}_i$ is the position of atom i, and $\langle \mathbf{r}_i \rangle$ denotes configurational average. The value of 4.5 is used for a' and is obtained from established simulation work that determined that this parameter is relatively independent of temperature and different proteins.[58] Determination of the Lindemann criterion provides a basis as to whether systems exhibit either solid-like or liquid-like properties. From previous simulation data, solid-like behavior is observed at $\Delta_L < 0.14$, and liquid-like characteristics are observed at $\Delta_L > 0.14$.[58] Although the range of values calculated from our studies is within solid-like behavior, our interpretation of the data is based on the relative values considering that the parameter is dependent on the total number of atoms, which may affect the actual magnitude.

3. RESULTS AND DISCUSSION

The chemical sequence of the four PA molecules is shown in Table 1 with three distinct regions: a hydrophobic palmitic alkyl tail, six-residue β-sheet forming region of valines and/or alanines, and a negatively charged group of three glutamic acids. **PA1** and **PA2** have identical chemical composition but different position of the hydrophobic residues, valine and alanine, in the β-sheet forming region. **PA3** and **PA4** are complementary sequences designed to examine the effects of using a homogeneous β-sheet forming segment that is either strongly or mildly hydrophobic. For the purpose of this paper, **PA1** and **PA2** will be primarily discussed in more details than **PA3** and **PA4**, whose additional data and analysis are presented as Supporting Information.

Our coarse-grained ePRIME model has been previously validated for use in self-assembly study on **PA1**.[42] We performed replica-exchange simulations using both atomistic CHARMM 27 force field[59−61] and ePRIME models to examine the effect of temperature on the folding process of a single **PA1** molecule. Equilibrium results showed that both coarse-grained and all-atom models produce similar conformations over a wide range of temperatures.[42] For this paper, we have performed an additional validation study on **PA2** obtaining high agreement between ePRIME and CHARMM results on not only the secondary structure formed by the peptide segment as a function of temperature, but also the interactions between the alkyl tail and the peptide segment (Figure S1).

In addition, we have performed a more detailed study previously[56] on peptide folding by **PA1** and **PA2** using the atomistic CHARMM model.[59−61] The alkyl tail was observed to play two opposing roles in modulating sequence-dependent folding kinetics and thermodynamics. On one hand, it restricts conformational freedom reducing the entropic cost of folding, which is thus promoted. On the other hand, it acts as an interaction site with nonpolar peptide residues, blocking the peptide from helix nucleation, which reduces folding. It was identified that the first critical event of folding kinetics requires

DOI: 10.1021/acs.biomac.5b00595
Biomacromolecules XXXX, XXX, XXX−XXX

creating a 3_{10}-helical turn, which involves alanine residues and later switches into a α-helical turn. **PA2** alanines experience 1.4 times as many van der Waals interactions with the alkyl tail compared to **PA1** alanines since they are closer to the alkyl tail. The high frequency of tail−peptide interactions prevents the peptide from folding in **PA2** relative to **PA1**. When the alkyl tail was truncated to four immobile carbon groups, disruptive hydrophobic interactions are reduced to enable higher rates of folding.

3.1. Switching Placement of Hydrophobic Peptide Residue Blocks Yield Nanostructures with Contrasting Structural Arrangements. Starting from initial configurations containing 800 PA molecules in random coil conformations at a moderate temperature of $T^* = 0.11$, spontaneous self-assembly occurs resulting in the formation of nanofiber structures with an elongated, high-aspect ratio geometric profile by both sequences **PA1** and **PA2**. Representative equilibrium self-assembled structures of **PA1** and **PA2** are shown in Figure 1A and 1B, respectively. Both

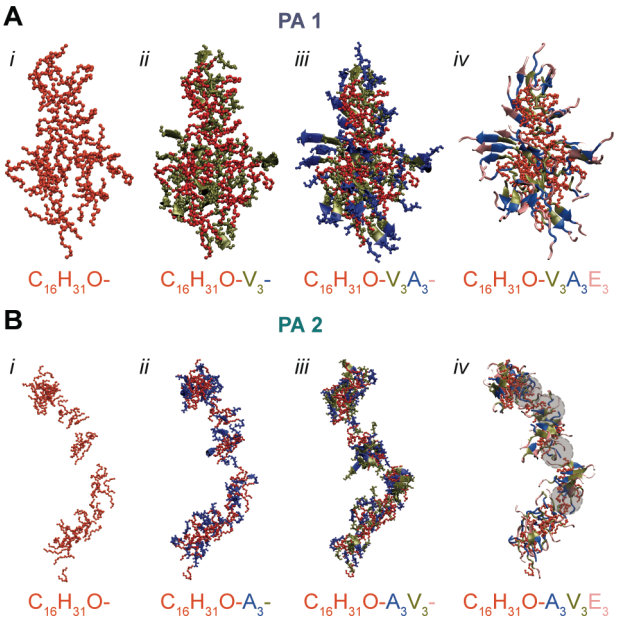

Figure 1. Representative equilibrium structure of cylindrical nanofibers showcasing (i) only the alkyl tails, (ii) plus the next three residues, (iii) plus another three residues, and (iv) the whole sequence of (A) **PA1** and (B) **PA2**. Color scheme using VMD:[62] alkyl tail (red), valine (green), alanine (blue), and glutamic acid (pink).

structures are comprised primarily of hydrophobic alkyl tails shielded by charged peptide segments. Formation of β-sheet secondary structure is evident along the surface of each nanostructure. However, upon detailed inspection, the internal spatial arrangement of these two structural analogues with identical chemical composition is noticeably different. By visually isolating the alkyl tails, the local organization of the collected assembly is highlighted to showcase that the interior hydrophobic core of PA1 cylindrical nanofiber is contiguous (Figure 1Ai). In contrast, the interior hydrophobic core of **PA2** cylindrical nanofiber has multiple discontinuous junctions (Figure 1Bi).

For **PA1**, a contiguous inner hydrophobic core comprises predominantly of alkyl tails are arranged in a compact form to maximize alkyl−alkyl interactions. In addition, adjacent hydrophobic residues, valine residues, are intertwined with the alkyl tails to strengthen the hydrophobic interactions (Figure 1Aii and Figure 1Aiii). This can be seen by the relatively high number of intermolecular hydrophobic interactions between the alkyl tail on each PA molecule and the first three peptide residues (i.e., valines for **PA1**) on nearby PA molecules as shown in Figure 2A.

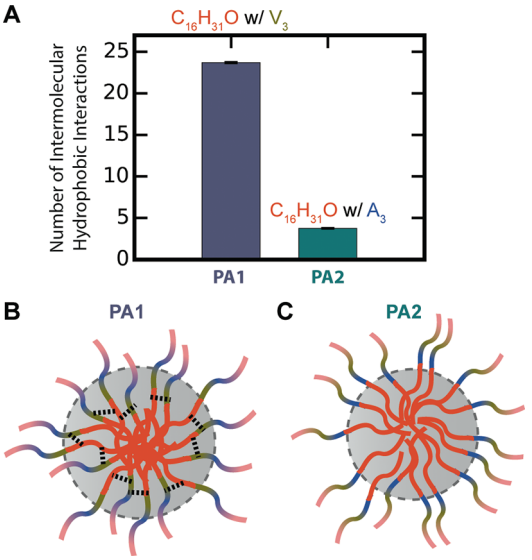

Figure 2. (A) Average number of intermolecular hydrophobic interactions between the alkyl tail of each PA molecule and the first three residues adjacent to the alkyl tail of a neighboring PA molecule within the interior of cylindrical nanofibers in **PA1** and **PA2** systems. Schematic diagram showing a cross-sectional view of typical cylindrical nanofibers (perpendicular to the elongated direction) illustrating the data shown in panel A for (B) PA1 and (C) PA2. Those intermolecular hydrophobic interactions are shown as black dashed lines. Color scheme in diagram B and diagram C: alkyl tail (red), valine (green), alanine (blue), and glutamic acid (pink).

In contrast, **PA2** cylindrical nanofiber contain multiple micelles that are interconnected at discontinuous junctions (Figure 1B). The inner hydrophobic core of each micelle is comprised of only alkyl tails without pulling the first three peptide residues (i.e., mildly hydrophobic alanines for **PA2**) into the interior. This results in the relatively low number of intermolecular hydrophobic interactions between the alkyl tail on each PA molecule and alanines on nearby PA molecules as shown in Figure 2A. Moreover, about 15% molecules in **PA2** cylindrical nanofibers adopt an opposite orientation in which the charged segment is located within the inner core to form hydrophobic interactions between valine residues with other alkyl tails in the interior. In this case, the alkyl tails of these inverted molecules form hydrophobic interactions with alanine and valine residues on other molecules to connect multiple micelles at discontinuous junctions. Furthermore, alanine and valine residues form hydrogen bonds between micelles as shown in Figure 1Bii and Biii. Therefore, multiple micelles are held together by a combination of hydrophobic interactions between nonpolar peptide residues and additional hydrogen bonds by those residues.

The large number of interactions between the alkyl tail and adjacent valine residues works together in **PA1** to condense and bind together creating a hydrophobic core that is not only composed of the alkyl tails but also strongly hydrophobic valine residues (Figure 2B). Since the strong hydrophobic residue

DOI: 10.1021/acs.biomac.5b00595
Biomacromolecules XXXX, XXX, XXX−XXX

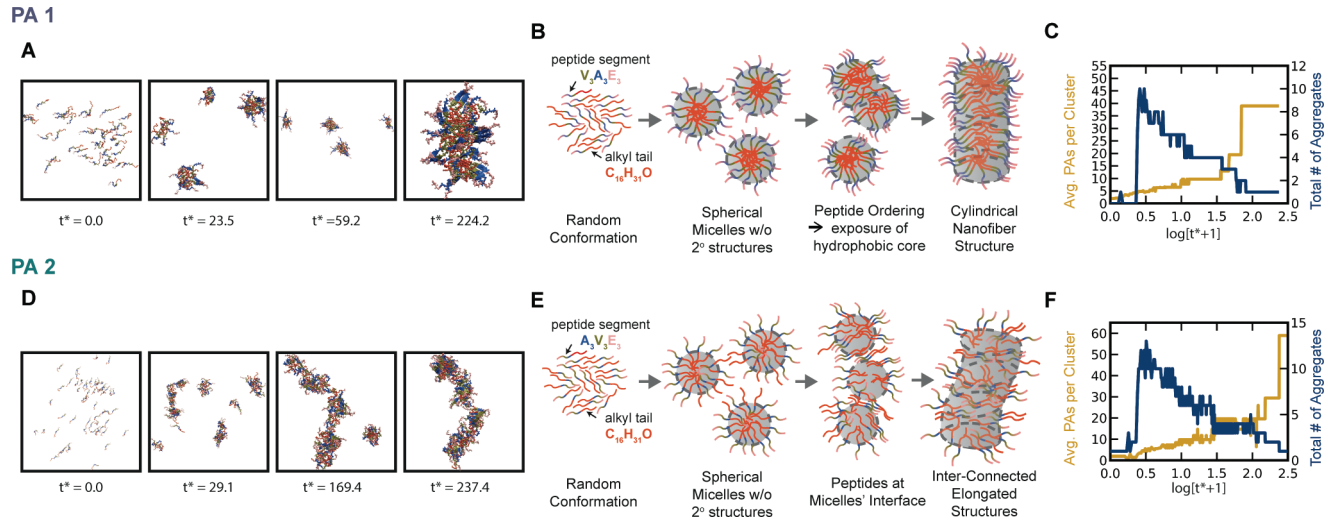

Figure 3. For **PA1**: (A) Snapshots showing dynamic self-assembly process at different times starting from random configurations; (B) schematic diagram generalizing a self-assembly kinetic mechanism for PA1 from multiple simulations; (C) time-dependent data are plotted on a logarithmic scale for the average number of PA molecules per aggregate and total number of aggregates. Similarly for **PA2**: (D) Snapshots, (E) schematic diagram, and (F) quantitative data.

group, valines, is placed farther away from the alkyl tail in **PA2**, alkyl tails form only a few intermolecular hydrophobic interactions with weakly hydrophobic alanine residues (Figure 2A). Therefore, the hydrophobic core is less compact since each alkyl tail would have to twist and extend itself to form interactions with valine residues (Figure 2C). By having a more porous hydrophobic core, the ability to form β-sheets diminishes since the peptide residues are no longer within optimal distance to promote intermolecular hydrogen bonding while minimizing charge−charge repulsion. This can be attributed to the observed difference in the macroscopic gel stiffness as discussed in subsequent sections.

3.2. Sequence-Dependent Structural Difference Is Caused by Dynamic Assembly Mechanisms. Through a series of micelle merging events, spontaneous self-assembly of PA molecules into a cylindrical nanofiber are shown in Figure 3 for **PA1** and **PA2**. For PA1, initial clusters of PA molecules adopt a spherical micelle configuration (Figure 3A) such that the charged glutamic acid residues are distributed uniformly to minimize electrostatic repulsions. The inner core is comprised of alkyl tails that are sequestered away from the surface. Upon the formation of intermolecular hydrogen bonds by the hydrophobic valine and alanine residues, the peptide segments on the surface of each micelle undergo an ordering process by forming multiple separate β-sheets. As a result, the hydrophobic core is exposed to the surface or solvent, which promotes merging with nearby micelles to grow into a cylindrical nanostructure. A schematic diagram in Figure 3B is shown to generalize a self-assembly kinetic mechanism for **PA1** from multiple simulations. The assembly mechanism can be interpreted from the plot shown in Figure 3C in which the average number of PAs increases in a stepwise process, whereas the total number of aggregates decreases in a reciprocating fashion. At each merging step, structural reorganization occurs allowing for maximizing the number of hydrophobic interactions within the core along the length of each elongated nanostructure, which grows into a longer nanofiber by adding more micelles at its two ends. Lateral growth of the nanofibril structure is limited due to the majority of charged glutamic acid segments residing on the side surface compared to its ends. Several key characteristics of the final structure (Figure 3A) are identified: alkyl tails with a large degree of entanglement are predominantly residing in the interior of the nanofiber, β-sheet forming perpendicular to the elongated core, and charged segments are scattered on the surface.

The early stage of the **PA2** self-assembly process is similar to that of **PA1** self-assembly (Figure 3D and Figure 3E). Starting from isolated molecules, **PA2** molecules quickly condense into small aggregates driven by hydrophobic collapse. As these small aggregates reach a size that is limited by the number of charged groups, subsequent steps for **PA2** aggregates to increase in size diverge from the already described **PA1** mechanism. In addition to micelle merging events that occur through the exposure of the hydrophobic core due to β-sheet formation, hydrophobic interactions between nonpolar groups on the surface of different micelles become more prominent. Since the strongly hydrophobic residue group of valine residues is placed farther away from the alkyl tail, the hydrophobic core of each micelle becomes less compact considering that the alkyl tail would have to twist and extend itself to form interactions with valine. Consequently, the inner core of each micelle adopts a different structural arrangement in which a few **PA2** molecules position in an opposite orientation with the charged segment located within the inner core while their alkyl tails are exposed to the surface. This allows connection between two nearby micelles by forming not only by hydrophobic alkyl−alkyl interaction but also by hydrophobic alkyl−side chain interaction and side chain−side chain interaction in addition to hydrogen bonds. This suggests that **PA2**'s discontinuous structure is seemingly held together through a combination of intermolecular hydrogen bonds and hydrophobic interactions at the interface of multiple smaller aggregates (Figure 3E). Subsequently, structural reorganization is less favored as indicated by absence of large plateaus in the plot of assembly kinetics (Figure 3F).

3.3. Molecular Arrangement of the Local Environment Influences the Internal Dynamics of the Nanostructure. Calculation of the amount of β-sheets (Figure 4A) shows that both **PA1** and **PA2** cylindrical nanofibers exhibit significantly large β-sheet formation at 24−30%, which is comparable to experimental results by Niece et al.,[12] who found

DOI: 10.1021/acs.biomac.5b00595
Biomacromolecules XXXX, XXX, XXX−XXX

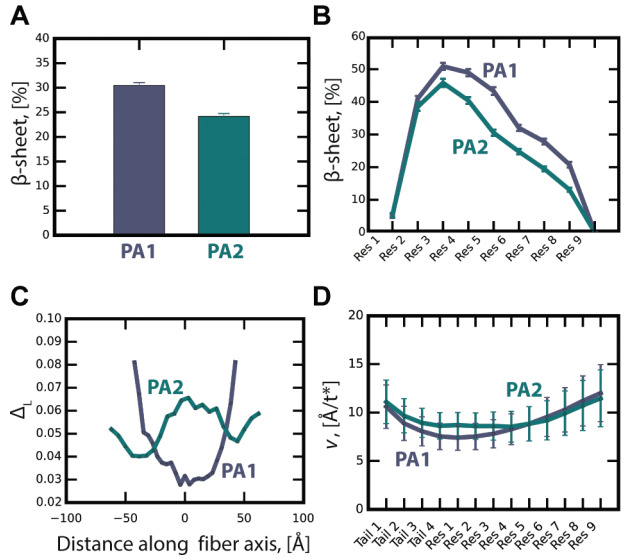

Figure 4. For both **PA1** and **PA2** cylindrical nanofibers at equilibrium: (A) Average amount of β-sheets. (B) The β-sheet propensity is plotted as a function of the peptide residue. (C) The Lindemann value at different points along the length of the fiber axis. (D) Average velocity of individual regions of each molecule. The first four regions correspond to the alkyl tail and remaining nine regions correspond to nine peptide residues.

the β-sheet population of similar PAs at ~25 ± 20%. Moreover, **PA1** has a slightly higher propensity to form β-sheets than **PA2** (Figure 4A). The significance of **PA2** having a weaker propensity to form a β-sheet compared to **PA1** may suggest a correlation to the 1 order of magnitude difference in bulk material properties as observed by Pashuck et al.[17] This has also been seen by other investigators who found that the formation of rod-like nanostructures is associated with the presence of hydrophobic residues with a strong propensity to form β-sheet structure; in addition, high amount of β-sheets correlates with stiffer hydrogel properties.[12,31,63]

However, the experimental study by Pashuck et al.[17] suggested that the β-sheet misalignment or twisting, instead of the amount of β-sheets, plays an important role in influencing the stiffness of the gel. In this case, each cylindrical nanofiber structure was assumed to contain multiple large β-sheets that are infinitely long, running continuously along the length of the fiber axis. However, prior experimental studies with similar PAs have quantified the amount of β-sheets to be approximately ~25 ± 20%,[12] which is in agreement with a modeling simulation study using atomistic models by Lee et al., who found the presence of sparsely distributed small β-sheets along the surface.[52] Nevertheless, we attempted to determine the degree of β-sheet twistedness by calculating the angles between one hydrogen bond to other hydrogen bonds within each β-sheet using PyMOL.[64] We found no significant difference of such angle distributions by β-sheets between **PA1** and **PA2** nanofibers (Figure S2). Perhaps the slightly lower β-sheet formation for **PA2** than **PA1** might be a potential factor for the experimental observation of a tremendous difference in mechanical property between **PA1** and **PA2**. Based on the structures shown, **PA2** is unable to maximize the formation of intermolecular hydrogen bonds due to the presence of 15% **PA2** molecules in an inverted orientation. Considering the increased propensity for peptide residues to form hydrophobic interactions at discontinuous junctions, the ability to form secondary structures is thereby inhibited. These factors not only result in a reduced amount of β-sheet structure, but also lead to a discontinuous hydrophobic core. Consequently, it is believed that the amount of β-sheets and the structural integrity of the hydrophobic core influence the mechanical property of the self-assembled nanofiber structure. To compare with this experimental speculation, we measured individual peptide residues likelihood to form β-sheet elements, and this is shown in Figure 4B. For **PA1**, residues 3−6 (-VAAA-) are shown to have a higher propensity to form β-sheets as compared to **PA2** for the residues in the same position (-AVVV-). This suggests that the ability for β-sheets for **PA2** is inhibited or unfavorable and could be related to the placement of the hydrophobic residues with respect to the alkyl tail.

In an attempt to provide a more quantitative and concrete correlation between the subtle difference between the arrangement of the inner core of **PA1** and **PA2** and their structural stability, we also calculated the Lindemann criterion. The dimensionless parameter can be interpreted as a value to represent the geometric packing or porosity of a structure. If the Lindemann value is large, it represents that the structure exhibits more liquid-like properties, whereas if the number is small, it exhibits more solid-like dynamics. From a previous simulation study, solid-like behavior is observed at $\Delta_L < 0.14$, and liquid-like characteristics are observed at $\Delta_L > 0.14$.[58] Although the range of Lindemann values calculated from our studies is within solid-like behavior, our interpretation of the data is based on the relative values considering that the parameter is dependent on the total number of atoms, which varies from one position to another and thereby may affect the actual magnitude. In Figure 4C, the Lindemann values are plotted as a function of position along the length of the fiber axis (or elongated dimension) of a representative nanostructure of **PA1** and **PA2**. Since the end groups are more flexible, comparison should be made between the two sequences at the central part of the nanostructures. In this case, a noticeable difference exists in the Lindemann values of **PA1** and **PA2**. Unlike **PA1** in which the structure shows increasingly more solid-like dynamics toward the core the structure, **PA2** shows an inverse trend: the core exhibit more liquid-like dynamics. This suggests that **PA1** structure becomes more condense and tighter corroborating with previous speculation due to the added hydrophobic interactions between the entangled alky tails and alkyl tail−valine interaction. Moreover, **PA2** experiences several large spikes that correlate with discontinuities observed along the inner hydrophobic core of a more porous structure.

To gain further insight and to account for the experimentally observed drastic difference in gel stiffness, dynamics of individual molecules of the collective assemblies are monitored. For **PA1** and **PA2**, each molecule is subdivided into a total of 13 sections with the first 4 sections representing four quarters of the alkyl tail and the remaining nine sections corresponding to each amino acid. For each of the aggregates in the system, the velocity was calculated for each section as shown in Figure 4D. The local molecular motion is largest at the ends of the alkyl tail (Tail 1−2) and at the negatively charged glutamic residues (Residue 7−9) for both **PA1** and **PA2**. The increased molecular motion of the glutamic acid residues can be attributed to the added flexibility as a result of their peripheral location on the surface. While the ends of the alkyl tails are buried within and shielded from the aqueous medium, they exhibit increased molecular motion due to their nature of

DOI: 10.1021/acs.biomac.5b00595
Biomacromolecules XXXX, XXX, XXX−XXX

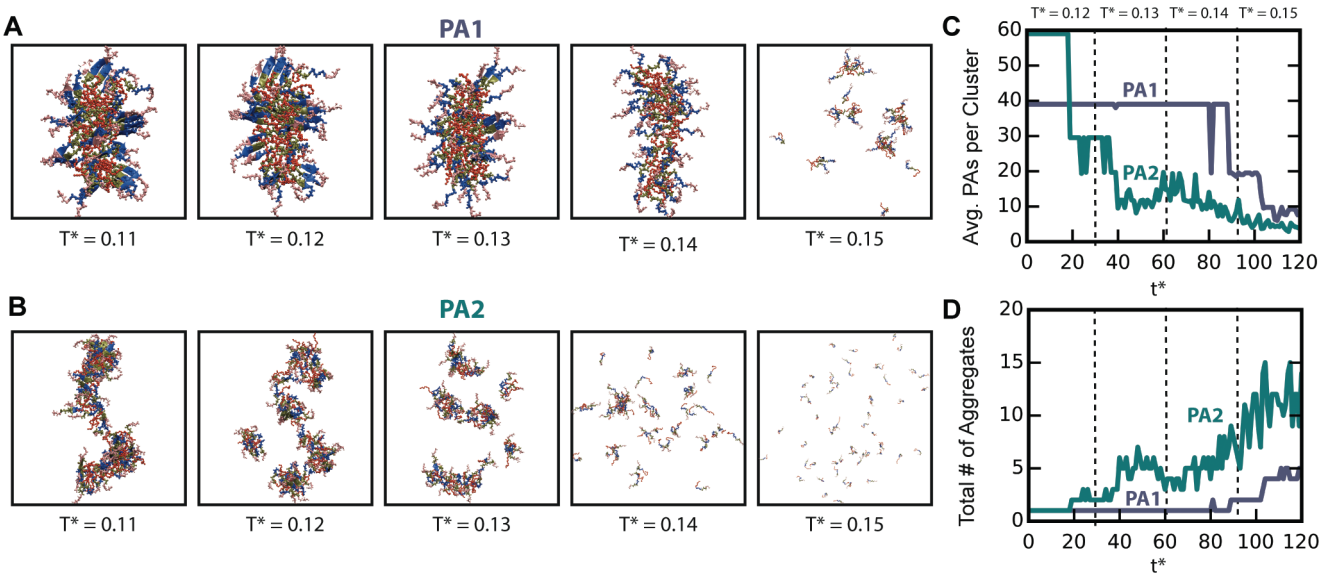

Figure 5. Snapshots of the equilibrated structure at the end of each temperature (T^* = 0.12−0.15) during the heating process for (A) **PA1** and (B) **PA2** starting from cylindrical nanofiber structures assembled at T^* = 0.11. (C) Plot of the average number of PA molecules per cluster as a function of time for **PA1** and **PA2**. (D) Plot of the total number of aggregates as a function of time for **PA1** and **PA2**. For panels C and D, heating intervals and heating temperatures are indicated by the dashed lines.

hydrophobic interactions, which are isotropic and thus easily broken up and reformed constantly. This allows them to move around without overcoming any energetic barrier. In contrast, a slight decrease in the calculated velocity is observed at positions Tail 3−4 and Residue 1−3, indicating that these groups of molecules are more restricted and experience less movement due to their nonisotropic interactions (i.e., hydrogen bonding) by the β-sheet-forming peptide residues. The aforementioned trends in the velocity are comparable to experimental findings by Ortony et al. using electron paramagnetic resonance spectroscopy to probe the internal dynamics of a nanofiber structure.[65] On one hand, solid-like dynamics were observed at the middle peptide region due to the significant amount of β-sheet formation that imposes structural order through directional dependent hydrogen bonding. On the other hand, fluid-like dynamics were observed at the surface and the core where alkyl tails exist. Faster dynamics at the periphery near charged residues were due to the reduced amount of hydrogen bonds, which decreases the rigidity of the architecture. Increased motion at the core is attributed to the flexibility of the end segment of the alkyl tails and their location that is a large distance away from the peptide residues.

3.4. Dissociative Properties of Assembled Aggregates Suggest a Correlation between Structural Stability and Mechanical Property. Assembled nanostructures that are strongly held together are expected to maintain their structural stability by resisting morphological changes even at high temperatures. Therefore, successive constant temperature simulations at increasing temperature were performed to investigate whether the structural differences between **PA1** and **PA2** have any direct influence on the mechanical properties of the collective assembly. Starting at the moderate temperature of T^* = 0.11, each system was subjected a temperature increase by an increment of T^* = 0.01 for about 30 reduced time units until the final temperature of T^* = 0.15 was reached. The time interval was chosen to provide a reasonable amount of time for the system to reach an equilibrated state before raising the temperature again. As seen in Figure 5A and 5B, the same structures from earlier **PA1** and **PA2** analysis is selected for continuity. In Figure 5A, snapshots of the equilibrated structure for **PA1** at the end of each heating interval is shown. For the selected structure, its ability to retain its structural framework over the course of the successive heating stages is noteworthy. Up to T^* = 0.14, the structure seems to stretch out due to the added kinetic energy such that the hydrophobic core becomes less entangled and more relaxed. Gradually, more hydrogen bonds are broken resulting in the dissociation of β-sheets as temperature increases; therefore, peptide segments switch from β-strand to random-coil conformation. However, the structure remains as an elongated micelle since the alkyl tails can still maintain their hydrophobic interactions. When the temperature is finally reached at T^* = 0.15, the structure is observed to undergo dissociation into smaller aggregates.

Unlike the nanostructure for **PA1**, the **PA2** nanostructure is more susceptible to dissociation even when the temperature is only slightly increased. From the snapshots shown in Figure 5B, at T^* = 0.12 the cylindrical nanofiber quickly dissociates into clusters that break into smaller aggregates. When the temperature reaches T^* = 0.15, the nanostructure has fully disintegrated into isolated random molecules. By plotting the average PAs per cluster as shown in Figure 5C, the aforementioned process for **PA1** and **PA2** can be differentiated by the rate at which the average number of PAs decreases over time. Throughout the heating process, **PA1** structure is relatively stable without losing its structure until an extremely high temperature is reached. By contrast, the plot for **PA2** shows sharp decreases indicating the structure is rapidly dissociating. The total number of aggregates is also monitored (Figure 5D) as a function of time and supports previous findings by mirroring the data shown in Figure 5C. As the temperature increases, the rate at which the total number of aggregates increases is much faster than **PA1**. These results confirm our finding based on the Lindemann criterion that structural stability of **PA1** nanofibers is higher than that of the **PA2** counterpart.

DOI: 10.1021/acs.biomac.5b00595
Biomacromolecules XXXX, XXX, XXX−XXX

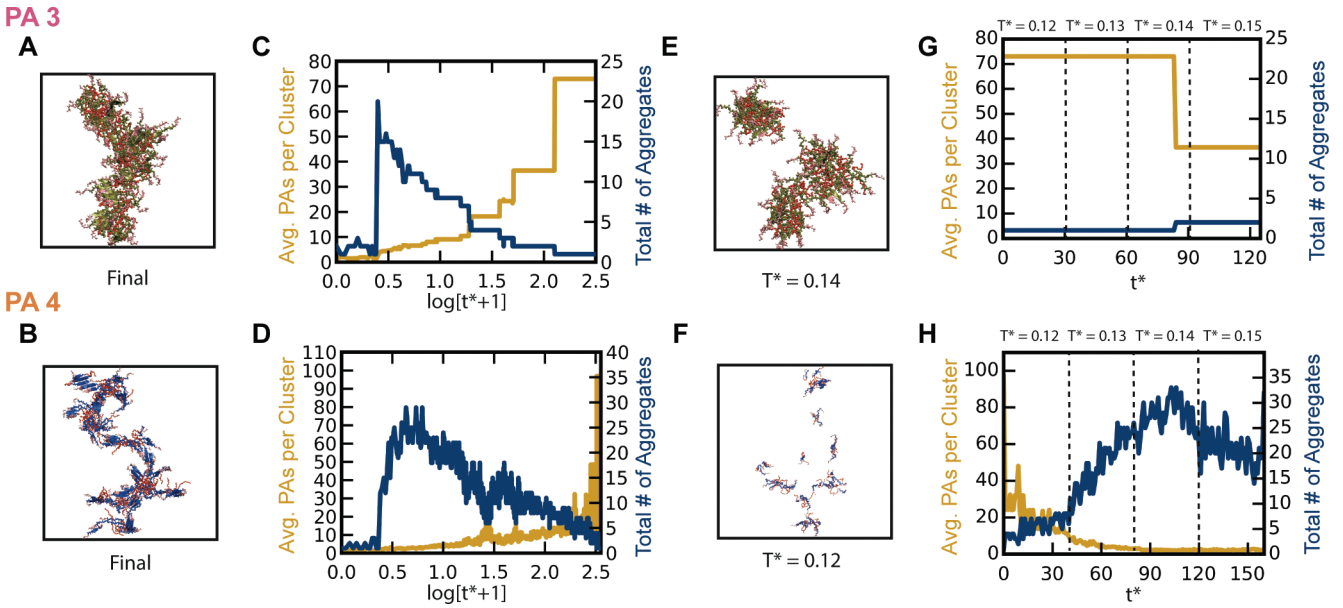

Figure 6. Snapshot of the equilibrated structure for (A) **PA3** and (B) **PA4** cylindrical nanofibers. Assembly kinetics with respect to the average number of PAs per cluster and total number of aggregates is plotted as a function of time for (C) **PA3** and (D) **PA4**. Snapshot of (E) **PA3** and (F) **PA4** nanostructure at the temperature at which the structure starts to dissociate. Dissociation kinetics with respect to the average number of PAs per cluster and total number of aggregates is plotted as a function of time for (G) **PA3** and (H) **PA4** during the heating process. The heating intervals and temperature are indicated by dashed lines.

3.5. Composition and Residue Order of PA Sequence Affect PA Self-Assembly and Structural Stability. In addition to examining positional influence on the self-assembly behavior of PA molecules, the effect of increasing the length of a single peptide residue that is either strongly or mildly hydrophobic to yield a homogeneous β-sheet forming segment was also studied for a more comprehensive understanding. **PA3** and **PA4** contain the same number of residues as **PA1** and **PA2**; however, instead of having two different residues in the β-sheet forming region, the β-sheet forming segment has been replaced to contain only either valine or alanine residues. **PA3** assembly results in the formation of cylindrical nanofibers. From Figure 6A and Figure S3A, the equilibrated structure for **PA3** resembles **PA1** in adopting an elongated shape with a continuous hydrophobic core comprise of alkyl tails. While valine residues are known for high propensity for β-sheet formation,[66] the percentage of β-sheets of **PA3** is 8% lower than that that of **PA1** (Figure S4A,B). As observed from its structure (Figure 6A and Figure S3A), the increased hydrophobic interaction between the alkyl tail and the valine side chain takes precedence over the likelihood to form hydrogen bonds since valine residues are strongly hydrophobic. Consequently, the structure is observed to be more compact with the valine residues being withdrawn into the hydrophobic core.

When the β-sheet forming region is only of alanine residues for **PA4**, the self-assembled nanostructure resembles **PA2** cylindrical structure with the exception of added junctions and more discontinuities along the inner core (Figure 6B and Figure S3B). Since alanine is known as weakly hydrophobic, the hydrophobic core is even less compact than that of **PA2** cylindrical nanofibers since the alkyl tail forms less hydrophobic interactions with alanine residues. Consequently, alanine residues are not withdrawn into the hydrophobic core. Instead they form the highest amount of hydrogen bonds and thus β-sheets (Figure S4A,B) over the other three sequences as expected.[66] Moreover, the increased propensity for intermolecular hydrogen bonds for **PA4** facilitate aggregate growth through added intermolecular hydrogen bonds creating more branched or disjointed junctions between micelles.

The assembly kinetics of **PA3** and **PA4** are shown in Figure 6C,D, respectively; details of the entire assembly mechanism are shown in Figure S5. The self-assembly mechanism of **PA3** is similar to that of **PA1**, while the self-assembly mechanism of **PA4** is similar to that of **PA2**.

Upon performing a heated simulation of these two systems, mechanical features can also be extrapolated based on their dissociation mechanism (Figure S6). Figure 6E,F show snapshots of **PA3** and **PA4** nanostructures at the temperatures where they start to disintegrate. Unlike **PA4** that immediately starts to dissociate into small clusters and individual molecules at $T^* = 0.12$, **PA3** nanostructure is much more robust and does not dissociate until higher temperatures of $T^* = 0.14$ (Figure S6). As shown in Figure 6G, **PA3** structure is considerably stable throughout the heating simulation. The stability is most likely attributed to the added hydrophobic interactions due to the presence of only valine residues that strengthen the core and outweighing the charge−charge repulsion from the glutamic acid residues. However, **PA4** is observed to be much more dynamic with the total number of aggregates quickly increasing indicative of the formation of small clusters (Figure 6H). Since disjointed micelles are weakly interconnected at multiple junctions, **PA4** nanostructure is more susceptible to disruptions by a slight temperature increase. Indeed, **PA4** nanostructures exhibit the most liquid-like dynamics, while **PA3** nanostructures exhibit the most solid-like dynamics even when being compared with **PA1** and **PA2** nanostructures based on the Lindemann parameter (Figure S7A) and motion velocity (Figure S7B).

DOI: 10.1021/acs.biomac.5b00595
Biomacromolecules XXXX, XXX, XXX−XXX

4. CONCLUSIONS

By simply interchanging the position of two blocks of hydrophobic residues (**PA1**: palmitoyl-$V_3A_3E_3$ and **PA2**: palmitoyl-$A_3V_3E_3$) within the β-sheet forming region of a model PA molecule, rod-like structures with distinctive internal structural arrangements were self-assembled. Characteristics of a prototypical cylindrical nanofiber structure of **PA1** is identified by the ability of the alkyl tails to pull the valine residues into the interior of the nanostructure to promote intermolecular hydrophobic interactions between the alkyl tail of a PA molecule with the first three peptide residues (i.e., valines) on nearby PA molecules. The hydrophobic core of **PA1** cylindrical nanofibers is therefore dense and contiguous containing not only the alkyl tails but also of valine residues. By contrast, the alkyl tails of PA2 molecules form significantly less intermolecular hydrophobic interactions between the alkyl tail of a PA molecule and the first three peptide residues (i.e., weakly hydrophobic alanines) of nearby PA molecules. Therefore, the hydrophobic core of **PA2** cylindrical nanofibers contains only the alkyl tails. Moreover, there are additional hydrophobic interactions between the alkyl tail of inverted molecules and valine residues, and hydrogen bonds that bridge the interface between micelles along the length of **PA2** fiber axis. Since the peptide residues of **PA2** form an increased number of hydrophobic interactions at the interface, the total number of hydrogen bonds that can be formed is subsequently reduced resulting in a lower propensity of β-sheet formation. While **PA1** and **PA2** forms sufficient β-sheet structures to promote one-dimensional self-assembled structures, calculation of the Lindemann parameter indicates that **PA2** nanofibers are structurally less stable than PA1 counterparts. Both **PA1** and **PA2** nanofibers were then subjected to temperature increases during a heating process showing that as the temperature increased from T^* = 0.12 to 0.15, the rate at which **PA2** dissociated into isolated random coil is much faster than **PA1**. These findings demonstrate a strong correlation with previous experimental work showing **PA2** exhibiting weaker mechanical properties than **PA1**.[17]

Compared to the experimental speculation that **PA2** forms an increased amount of misaligned hydrogen bonds and twisted β-sheets, our simulation results suggest that the reduced amount of β-sheets and the arrangement of hydrophobic core are mainly responsible for the observed decrease in macroscopic bulk material property. This observation is comparable to previous simulation results by Lee et al.,[53] who demonstrated that the difference in mechanical property between palmitoyl-$V_2A_4E_3$ and palmitoyl-$V_4A_2E_3$ is not β-sheet twistedness since each β-sheet is not infinitely continuous along the length of the fiber axis, as proposed by Stupp and co-workers,[17] but rather small in size containing 2−5 peptides as similarly observed in our simulations. Additional study on two more sequences (**PA3**: palmitoyl-V_6E_3 and **PA4**: palmitoyl-A_6E_3) to examine the effect of having a homogeneous sequence that is either strongly or mildly hydrophobic for the β-sheet forming region was performed in this study. Our results indicate the formation of two unique self-assembled nanostructures: elongated micelles and disjointed cylindrical micelles. Comparing all four sequences, it is shown that the balance between noncovalent interactions is immensely significant. As the β-sheet forming peptide region become less hydrophobic as in the case of **PA4**, the ability to form stable one-dimensional nanofiborus structure with contiguous hydrophobic core is limited. This agrees with our previous studies that examine the effects of solvent-dependent hydrophobicity[44,45] and to some extent pH-dependent electrostatics[10,42] on PA self-assembly.

Recently, Goldberger and co-workers investigated the role of positioning a strong β sheet-forming residue, isoleucine, relative to the alkyl tail on PA self-assembly.[8] They showed that moving this hydrophobic amino acid away from the alkyl tail induces nanofiber formation at lower concentrations and more basic pH values. The reason is that when one isoleucine is placed next to the alkyl tail, it forms attractive interactions with the alkyl tails of neighboring molecules, which hinders its β-sheet formation. Therefore, moving isoleucine away from the alkyl tail increases attractive interactions between peptide segments and subsequently promotes hydrogen bonds, which induces nanofiber formation at lower concentrations. Moreover, moving isoleucine closer to the charged glutamic acids also reduces electrostatic repulsion of those glutamic acids, which induces expansion of the pH range for nanofiber formation. Several key differences are present between their sequences and those sequences that were examined in our study. Their sequences are shorter in length by one residue yet containing an extra negatively charged glutamic acid. This reduces the number of β-sheet forming residues to four compared to six in our sequences. In addition, their sequence modification in the β-sheet domain involves only one residue as opposed to a block of three residues as in our study that shows that moving three valine residues closer to the charge glutamic acids overwhelmingly reduces the electrostatically repulsive character. This allows many **PA2** molecules to arrange themselves in an inverted orientation compared to the rest of **PA2** chains; indeed, 15% molecules in **PA2** cylindrical nanofibers adopt an opposite orientation in which the charged segment is located within the inner core to form hydrophobic interactions between their valine residues with other alkyl tails in the interior. This hypothesis can be further tested by performing additional simulation studies on those sequences examined by the Goldberger group.

Through this study, adjusting the position of individual residues may provide an alterative pathway to achieve desirable structural and functional characteristics for the development of innovative biomaterials in a more fine-tuning manner. This would allow using molecular simulations to aid in the design and development of bioinspired materials for the fields of drug delivery, diagnostic medicine, tissue engineering, and regenerative medicine

■ ASSOCIATED CONTENT

Supporting Information

Equilibrium conformations as a function of temperature for **PA1** and **PA2**, alignment of β-sheet data for **PA1** and **PA2**, and additional data for **PA3** and **PA4** are provided in the Supporting Information. The Supporting Information is available free of charge on the ACS Publications website at DOI: 10.1021/acs.biomac.5b00595.

■ AUTHOR INFORMATION

Corresponding Author

*Address: Department of Chemical Engineering and Materials Science University of California, Irvine, Irvine, California 92697-2575.

DOI: 10.1021/acs.biomac.5b00595
Biomacromolecules XXXX, XXX, XXX−XXX

Author Contributions

I.W.F and H.D.N. designed the research, I.W.F performed the simulations and the analysis, and I.W.F and H.D.N. wrote the paper. All authors have given approval to the final version of the manuscript.

Notes

The authors declare no competing financial interest.

■ ACKNOWLEDGMENTS

H.D.N. acknowledges financial support from UC Irvine. I.W.F. acknowledges support from a Graduate Research Fellowship from the National Science Foundation (DGE-1321846). This work used the Extreme Science and Engineering Discovery Environment (XSEDE), which is supported by National Science Foundation grant number OCI-1053575. We are also thankful for the computational resources provided by the GreenPlanet and High Performance Computing clusters at the UCI campus.

■ ABBREVIATIONS

PA, peptide amphiphiles; MD, molecular dynamics; VMD, Visual Molecular Dynamics

■ REFERENCES

(1) Dirks, A. T. J.; Nolte, R. J. M.; Cornelissen, J. J. L. M. *Adv. Mater.* **2008**, *20*, 3953−3957.
(2) Hartgerink, J. D.; Beniash, E.; Stupp, S. I. *Science* **2001**, *294*, 1684−1688.
(3) Trent, A.; Marullo, R.; Lin, B.; Black, M.; Tirrell, M. *Soft Matter* **2011**, *7*, 9572−9582.
(4) Tysseling-Mattiace, V. M.; Sahni, V.; Niece, K. L.; Birch, D.; Czeisler, C.; Fehlings, M. G.; Stupp, S. I.; Kessler, J. A. *J. Neurosci.* **2008**, *28*, 3814−3823.
(5) Sohdi, A.; Campbell, D.; Topham, P. *Chiang Mai J. Sci.* **2012**, *39*, 351−372.
(6) Pettikiriarachchi, J. T. S.; Parish, C. L.; Shoichet, M. S.; Forsythe, J. S.; Nisbet, D. R. *Aust. J. Chem.* **2010**, *63*, 1143−1154.
(7) Ghosh, A.; Haverick, M.; Stump, K.; Yang, X.; Tweedle, M. F.; Goldberger, J. E. *J. Am. Chem. Soc.* **2012**, *134*, 3647−3650.
(8) Ghosh, A.; Dobson, E. T.; Buettner, C. J.; Nicholl, M. J.; Goldberger, J. E. *Langmuir* **2014**, *30*, 15383−15387.
(9) Frisch, H.; Besenius, P. *Macromol. Rapid Commun.* **2015**, *36*, 346−363.
(10) Cote, Y.; Fu, I. W.; Dobson, E. T.; Goldberger, J. E.; Nguyen, H. D.; Shen, J. K. *J. Phys. Chem. C* **2014**, *118*, 16272−16278.
(11) Hartgerink, J. D.; Beniash, E.; Stupp, S. I. *Proc. Natl. Acad. Sci. U. S. A.* **2002**, *99*, 5133−5138.
(12) Niece, K. L.; Czeisler, C.; Sahni, V.; Tysseling-Mattiace, V.; Pashuck, E. T.; Kessler, J. A.; Stupp, S. I. *Biomaterials* **2008**, *29*, 4501−4509.
(13) Toksoz, S.; Mammadov, R.; Tekinay, A. B.; Guler, M. O. *J. Colloid Interface Sci.* **2011**, *356*, 131−137.
(14) Yu, Y.-C.; Berndt, P.; Tirrell, M.; Fields, G. B. *J. Am. Chem. Soc.* **1996**, *118*, 12515−12520.
(15) Black, M.; Trent, A.; Kostenko, Y.; Lee, J. S.; Olive, C.; Tirrell, M. *Adv. Mater.* **2012**, *24*, 3845−3849.
(16) He, C.; Han, Y.; Fan, Y.; Deng, M.; Wang, Y. *Langmuir* **2012**, *28*, 3391−3396.
(17) Pashuck, E. T.; Cui, H.; Stupp, S. I. *J. Am. Chem. Soc.* **2010**, *132*, 6041−6046.
(18) Cui, H.; Cheetham, A. G.; Pashuck, E. T.; Stupp, S. I. *J. Am. Chem. Soc.* **2014**, *136*, 12461−12468.
(19) Storrie, H.; Guler, M. O.; Abu-Amara, S. N.; Volberg, T.; Rao, M.; Geiger, B.; Stupp, S. I. *Biomaterials* **2007**, *28*, 4608−4618.
(20) Dagdas, Y. S.; Tombuloglu, A.; Tekinay, A. B.; Dana, A.; Guler, M. O. *Soft Matter* **2011**, *7*, 3524−3532.
(21) Ghanaati, S.; Webber, M. J.; Unger, R. E.; Orth, C.; Hulvat, J. F.; Kiehna, S. E.; Barbeck, M.; Rasic, A.; Stupp, S. I.; Kirkpatrick, C. J. *Biomaterials* **2009**, *30*, 6202−6212.
(22) Dehsorkhi, A.; Castelletto, V.; Hamley, I. W. *J. Pept. Sci.* **2014**, *20*, 453−467.
(23) Cui, H.; Webber, M. J.; Stupp, S. I. *Biopolymers* **2010**, *94*, 1−18.
(24) Jun, H.-W.; Paramonov, S. E.; Dong, H.; Forraz, N.; McGuckin, C.; Hartgerink, J. D. *J. Biomater. Sci., Polym. Ed.* **2008**, *19*, 665−676.
(25) Kim, J.-K.; Anderson, J.; Jun, H.-W.; Repka, M. A.; Jo, S. *Mol. Pharmaceutics* **2009**, *6*, 978−985.
(26) Khan, S.; Sur, S.; Newcomb, C. J.; Appelt, E. A.; Stupp, S. I. *Acta Biomater.* **2012**, *8*, 1685−1692.
(27) Klok, H.-A. *J. Polym. Sci., A: Polym. Chem.* **2004**, *43*, 1−17.
(28) Engler, A. J.; Sen, S.; Sweeney, H. L.; Discher, D. E. *Cell* **2006**, *126*, 677−689.
(29) Tse, J. R.; Engler, A. J. *Preparation of Hydrogel Substrates with Tunable Mechanical Properties*; John Wiley & Sons, Inc.: Hoboken, NJ, 2001.
(30) Discher, D. E.; Janmey, P.; Wang, Y.-L. *Science* **2005**, *310*, 1139−1143.
(31) Paramonov, S. E.; Jun, H.-W.; Hartgerink, J. D. *J. Am. Chem. Soc.* **2006**, *128*, 7291−7298.
(32) Yan, C.; Pochan, D. J. *Chem. Soc. Rev.* **2010**, *39*, 3528−3540.
(33) Schneider, J. P.; Pochan, D. J.; Ozbas, B.; Rajagopal, K.; Pakstis, L.; Kretsinger, J. *J. Am. Chem. Soc.* **2002**, *124*, 15030−15037.
(34) Roberts, D.; Rochas, C.; Saiani, A.; Miller, A. F. *Langmuir* **2012**, *28*, 16196−16206.
(35) Ramachandran, S.; Trewhella, J.; Tseng, Y.; Yu, Y. B. *Chem. Mater.* **2006**, *18*, 6157−6162.
(36) Ramachandran, S.; Yu, Y. B. *BioDrugs* **2006**, *20*, 263−269.
(37) Ramachandran, S.; Tseng, Y.; Yu, Y. B. *Biomacromolecules* **2005**, *6*, 1316−1321.
(38) Meng, Q.; Kou, Y.; Ma, X.; Liang, Y.; Guo, L.; Ni, C.; Liu, K. *Langmuir* **2012**, *28*, 5017−5022.
(39) Yuwono, V. M.; Hartgerink, J. D. *Langmuir* **2007**, *23*, 5033−5038.
(40) Wang, J.; Han, S.; Meng, G.; Xu, H.; Xia, D.; Zhao, X.; Schweins, R.; Lu, J. R. *Soft Matter* **2009**, *5*, 3870−3878.
(41) Missirlis, D.; Chworos, A.; Fu, C. J.; Khant, H. A.; Krogstad, D. V.; Tirrell, M. *Langmuir* **2011**, *27*, 6163−6170.
(42) Fu, I. W.; Markegard, C. B.; Chu, B. K.; Nguyen, H. D. *Adv. Healthcare Mater.* **2013**, *2*, 1388−1400.
(43) Morriss-Andrews, A.; Shea, J.-E. *Annu. Rev. Phys. Chem.* **2015**, *66*, 643−666.
(44) Fu, I. W.; Markegard, C. B.; Chu, B. K.; Nguyen, H. D. *Langmuir* **2014**, *30*, 7745−7754.
(45) Fu, I. W.; Markegard, C. B.; Nguyen, H. D. *Langmuir* **2015**, *31*, 315−324.
(46) Voegler Smith, A.; Hall, C. K. *Proteins: Struct., Funct., Bioinf.* **2001**, *44*, 344−360.
(47) Nguyen, H. D.; Hall, C. K. *Proc. Natl. Acad. Sci. U. S. A.* **2004**, *101*, 16180−16185.
(48) Nguyen, H. D.; Marchut, A. J.; Hall, C. K. *Protein Sci.* **2004**, *13*, 2909−2924.
(49) Wallqvist, A.; Ullner, M. *Proteins: Struct., Funct., Bioinf.* **1994**, *18*, 267−280.
(50) Wesson, L.; Eisenberg, D. *Protein Sci.* **1992**, *1*, 227−235.
(51) Gu, W.; Rahi, S. J.; Helms, V. *J. Phys. Chem. B* **2004**, *108*, 5806−5814.
(52) Lee, O.-S.; Stupp, S. I.; Schatz, G. C. *J. Am. Chem. Soc.* **2011**, *133*, 3677−3683.
(53) Lee, O.-S.; Liu, Y.; Schatz, G. C. *J. Nanopart. Res.* **2012**, *14*, 1−7.
(54) Lee, O.-S.; Cho, V.; Schatz, G. C. *Nano Lett.* **2012**, *12*, 4907−4913.
(55) Andersen, H. C. *J. Chem. Phys.* **1980**, *72*, 2384−2393.
(56) Chu, B. K.; Fu, I. W.; Markegard, C. B.; Choi, S. E.; Nguyen, H. D. *Biomacromolecules* **2014**, *15*, 3313−3320.
(57) Frishman, D.; Frishman, D.; Argos, P.; Argos, P. *Proteins: Struct., Funct., Bioinf.* **1995**, *23*, 566−579.

DOI: 10.1021/acs.biomac.5b00595
Biomacromolecules XXXX, XXX, XXX−XXX

(58) Zhou, Y.; Zhou, Y.; Vitkup, D.; Vitkup, D.; Karplus, M.; Karplus, M. *J. Mol. Biol.* **1999**, *285*, 1371−1375.
(59) MacKerell, A. D., Jr.; Bashford, D.; Bellott, M.; Dunbrack, R. L., Jr; Evanseck, J. D.; Field, M. J.; Fischer, S.; Gao, J.; Guo, H.; Ha, S. *J. Phys. Chem. B* **1998**, *102*, 3586−3616.
(60) Mackerell, A. D., Jr.; Feig, M.; Brooks, C. L., III. *J. Comput. Chem.* **2004**, *25*, 1400−1415.
(61) Brooks, B. R.; Brooks, C. L., III; MacKerell, A. D., Jr.; Nilsson, L.; Petrella, R. J.; Roux, B.; Won, Y.; Archontis, G.; Bartels, C.; Boresch, S.; Caflisch, A.; Caves, L.; Cui, Q.; Dinner, A. R.; Feig, M.; Fischer, S.; Gao, J.; Hodoscek, M.; Im, W.; Kuczera, K.; Lazaridis, T.; Ma, J.; Ovchinnikov, V.; Paci, E.; Pastor, R. W.; Post, C. B.; Pu, J. Z.; Schaefer, M.; Tidor, B.; Venable, R. M.; Woodcock, H. L.; Wu, X.; Yang, W.; York, D. M.; Karplus, M. *J. Comput. Chem.* **2009**, *30*, 1545−1614.
(62) Humphrey, W.; Dalke, A.; Schulten, K. *J. Mol. Graphics* **1996**, *14*, 33−38.
(63) Stendahl, J. C.; Rao, M. S.; Guler, M. O.; Stupp, S. I. *Adv. Funct. Mater.* **2006**, *16*, 499−508.
(64) The PyMOL Molecular Graphics System, Version 1.7.4; Schrödinger, LLC.
(65) Ortony, J. H.; Newcomb, C. J.; Matson, J. B.; Palmer, L. C.; Doan, P. E.; Hoffman, B. M.; Stupp, S. I. *Nat. Mater.* **2014**, *13*, 812−816.
(66) Chou, P. Y.; Fasman, G. D. *Biochemistry* **1974**, *13*, 222−245.

DOI: 10.1021/acs.biomac.5b00595
Biomacromolecules XXXX, XXX, XXX−XXX